Proteoform-Resolved Phosphorylation Dynamics in Kinase Complexes by Hybrid Precision Mass Spectrometry

Boris Krichel*[1,2,3,4,6], Hsin-Ju Chan[5], Liam Bandura[5], Zhan Gao[5], Man-Di Wang[5], Holden T. Rogers[5], Sean J. Mcilwain[7,8], Charlotte Uetrecht[4,6], and Ying Ge*[1,2,5]

[1] Department of Cell and Regenerative Biology, School of Medicine and Public Health, University of Wisconsin-Madison, Madison, Wisconsin, USA.

[2]Human Proteomics Program, School of Medicine and Public Health, University of Wisconsin-Madison, Madison, Wisconsin, USA.

[3] Faculty V: School of Life Sciences, University of Siegen, 57076 Siegen, Germany.

[4]CSSB Centre for Structural Systems Biology, Deutsches Elektronen Synchroton DESY, Leibniz Institute of Virology and University of Lübeck, Notkestraße 85, 22607 Hamburg, Germany.

[5]Department of Chemistry, University of Wisconsin-Madison, Madison, Wisconsin, USA.

[6]Institute of Chemistry and Metabolomics. University of Lübeck, 23562 Lübeck, Germany.

[7]Department of Biostatistics and Medical Informatics, University of Wisconsin-Madison, Madison, WI 53705, United States.

[8]University of Wisconsin Carbone Cancer Center, University of Wisconsin-Madison, Madison, WI 53705, United States.

*Corresponding authors: Dr. Boris Krichel: boris.krichel@cssb-hamburg.de; Dr. Ying Ge: ying.ge@wisc.edu

ABSTRACT

Protein phosphorylation creates functionally distinct proteoforms through complex modification cascades, yet capturing their temporal dynamics and combinatorial patterns remains a major analytical challenge. Here, we introduce a hybrid precision mass spectrometry (MS) strategy that integrates intact mass measurements for temporal proteoform tracking, bottom-up MS for site-specific kinetics, and top-down MS sequencing for proteoform characterization to resolve phosphorylation dynamics within intact kinase complexes. Applying this approach to AMP-activated protein kinase (AMPK, αβγ-complex) reveals that phosphorylation proceeds as a hierarchical proteoform cascade rather than a binary activation switch. We define dual entry mechanisms in which canonical CaMKK2-mediated or allosteric ADaM-site activation both trigger extensive autophosphorylation with α1-S496 showing the highest kinetic efficiency. Top-down MS sequencing uncovers channeled proteoform formation, exemplified by predominant β1-S24/25+S108 co-phosphorylation that links subcellular localization with allosteric responsiveness. Phosphatase competition reveals asymmetric control: PP1A removes activation-loop phosphorylation while autophosphorylation sites remain protected, establishing persistent regulatory states. This strategy resolves proteoform dynamics underlying kinase activation and provides a broadly applicable framework for studying phosphorylation-based regulation in therapeutic targets.

KEYWORDS

Proteoforms, Top-down mass spectrometry, AMPK, Phosphorylation, FTICR-MS

DATA AVAILABILITY

The mass spectrometry proteomics data generated in this study have been deposited to the ProteomeXchange Consortium via the MassIVE repository with identifier MSV000099446.

MAIN

Post-translational modifications (PTMs) expand the molecular diversity of the proteome far beyond its genetic blueprint, empowering proteins with the ability to adapt and regulate their functions dynamically[1,2]. Proteoforms, molecular variants arising from PTMs, alternative splicing, and genetic variation, underpin biological complexity[3,4]. Among the PTMs, phosphorylation creates functionally distinct proteoforms that regulate cellular signaling and metabolic homeostasis[5,6]. Elucidating how multiple phosphorylation sites collectively modulate protein function is essential for developing therapeutics targeting metabolic kinases, which control cellular energy homeostasis and represent promising drug targets for metabolic disorders including diabetes and obesity[7,8]. However, capturing the temporal dynamics and combinatorial patterns of these phosphorylations with analytical precision remains challenging[9,10].

Mass spectrometry (MS)-based proteomics has transformed phosphorylation research by enabling multiplexed and quantitative analysis with sequence-level resolution[11–14]. Bottom-up proteomics excels at deep proteome coverage and site identification through peptide level analysis, yet it disrupts the proteoforms and loses information on combinatorial modification patterns[15,16]. In contrast, top-down proteomics[17] preserves intact proteoform architectures and combinatorial modification patterns but with limited throughput and difficulty in mapping phosphorylation sites especially for large proteins[18,19]. For proteins with multiple phosphorylation sites and complex regulatory patterns, comprehensive proteoform-centric analysis requires integrating both approaches. Capturing how individual phosphorylation sites change over time while preserving their combinatorial patterns is critical because phosphorylation can occur in hierarchical cascades in which initial modifications gate subsequent events[20,21]. Experimental strategies must therefore integrate site-specific kinetics with intact proteoform measurements to resolve these dynamic regulatory mechanisms.

Herein, we introduce a hybrid precision mass spectrometry strategy that integrates quantitative intact mass measurements for temporal proteoform tracking, bottom-up analysis for site-specific phosphorylation kinetics and top-down sequencing for proteoform

characterization. We applied this hybrid strategy to human AMP-activated protein kinase (AMPK), a prototypical system that exemplifies the analytical challenge of resolving dynamic, multi-site phosphorylation[22,23]. This heterotrimeric complex (α-β-γ) functions as a central regulator of cellular energy metabolism with broad therapeutic relevance across metabolic, cardiovascular, and aging-related diseases[24–27]. AMPK is canonically known to require AMP binding and activation loop phosphorylation at α1-T183 by upstream kinases such as calcium/calmodulin dependent protein kinase kinase 2 (CaMKK2) to achieve catalytic activation and downstream substrate phosphorylation[28,29]. However, AMPK also undergoes extensive autophosphorylation, creating diverse proteoform landscapes whose regulatory roles and temporal relationships remain poorly defined[30,31]. Using our hybrid precision MS strategy, we uncover AMPK proteoform dynamics during activation, revealing how autophosphorylation creates diverse modification patterns at sites linked to distinct regulatory functions. These findings extend beyond the traditional binary activation model to define a dynamic and multi-mechanistic proteoform-centric activation model as well as establish a generalizable framework for analyzing therapeutic kinase targets.

RESULTS

A hybrid MS strategy enables proteoform-resolved phosphorylation dynamics

We developed a hybrid precision MS platform that unifies three complementary MS approaches to comprehensively characterize phosphorylation dynamics (Fig. 1a-c); Intact protein reverse phase liquid chromatography mass spectrometry (RPLC-MS) quantifies proteoform changes over time (Fig. 1a), bottom-up MS resolves site-specific phosphorylation kinetics (Fig. 1b), and top-down fragmentation using ultra high-resolution MS definitively identifies proteoform architectures through sequencing (Fig. 1c). This integrated approach addresses individual method limitations by combining intact mass, sequence information, and temporal dynamics in a unified analytical framework (Fig. 1d).

We applied this strategy to AMP activated protein kinase (AMPK), which exists as 12 possible heterotrimeric combinations through different isoforms (α1-2, β1-2 and γ1-3)[32]. We

produced full-length physiological α1β1γ1 isoforms in *E. coli*[33], the ubiquitously expressed isoform combination in human tissues, and purified the complex to homogeneity (Fig. 1e-f, Table S1). We activated AMPK using AMP and CaMKK2 mediated phosphorylation (Fig. 1g). AMPK functionality was validated through activity assays using synthetic SAMS peptide substrate which confirmed that the enzyme was functional with an EC50 = 12 nM, demonstrating quality comparable to commercial preparations (Fig. 1h)[34]. Time-resolved phosphorylation reactions were performed and were quenched at defined intervals for MS analysis (Fig. 1i).

AMPK subunits exhibit distinct phosphorylation profiles

AMPK subunits undergo differential phosphorylation with distinct temporal patterns. To quantify these dynamics, we performed *in vitro* phosphorylation of the AMPK complex using CaMKK2/Calmodulin. CaMKK2 represents a primary upstream kinase of AMPK, phosphorylating α1-T183 in the activation loop, resulting in about 100-fold activity enhancement[28]. To analyze phosphorylation status, we applied an intact protein RPLC-MS approach, providing highly reproducible chromatographic separation (Fig. 2a). Intact mass analysis of unphosphorylated AMPK subunits confirmed the expected molecular weights (Table S2).

Intact protein MS at the initial time point showed well-resolved charge state distributions (Fig. 2b, Fig. S1a). Deconvoluted mass analysis confirmed proteoform identification with high mass accuracy (Fig. 2c). Although we detected initial phosphorylation and mass heterogeneity through non-specific modifications known from *E. coli*[35] (Fig. 2d), the unphosphorylated species (0P) was by far the dominant form in all three subunits prior to CaMKK2 treatment, after which phosphorylation levels increased dramatically (Fig. 2e). Analysis of total phosphorylation (P_{total}) over 200 min revealed the sequential mass increase across AMPK subunits, culminating in the highest levels for α1 (5.33±0.04), intermediate for β1 (2.72±0.01), and minimal for γ1 (0.61±0.01) (Fig. 2f, extended validation in Fig. S1b).

Representative deconvoluted mass spectra across the time course demonstrate the sequential phosphorylation events (Fig. 2e). The maximum phosphorylation states observed at 200 min (α1: 7P, β1: 4P, γ1: 1P) represent the minimum number of phosphorylatable sites on each subunit, since not all sites reach full stoichiometric phosphorylation. Distribution of AMPK proteoforms throughout the spectra revealed distinct phosphorylation behaviors: α1 exhibited a broad, distributed envelope indicating multiple competing modification pathways, whereas β1 showed preferential accumulation at the P2 state, suggesting a more channeled phosphorylation pattern with one predominant proteoform.

While numerous phosphorylation sites have been reported for AMPK subunits[31,36–40] and prior intact MS studies have observed activation-dependent proteoform changes in α2β2γ3 complexes[41], our results reveal richer phosphorylation patterns than expected from direct CaMKK2 targeting alone, indicating triggered autophosphorylation cascades following initial α1-T183 activation. MS-based and biochemical studies report variable numbers of potential autophosphorylation sites (6 for α1, 7 for β1, none for γ1 based on PhosphoSitePlus compilation), although the specific sites and stoichiometry depend heavily on experimental conditions[42]. These quantitative phosphorylation profiles revealed distinct subunit-specific hierarchies, motivating investigation of the underlying regulatory mechanisms driving AMPK activation.

Phosphatase competition reveals selective targeting of activation sites

AMPK regulation involves a dynamic equilibrium between kinase-mediated phosphorylation and phosphatase-mediated dephosphorylation, with PP1A preventing constitutive activation[43]. Understanding which sites are preferentially targeted by phosphatases provides insight into AMPK's regulatory architecture.

We investigated the interplay through competitive phosphorylation-dephosphorylation reactions using increased PP1A concentrations (Fig. 3a). In the absence of PP1A, total phosphorylation after 100 min reached levels (α1: 4.44 ± 0.03P, β1: 2.34 ± 0.01P, γ1: 0.46 ± 0.01P) (Fig. S2a-c) comparable to previous experiments. However, even low PP1A (4.52 μM)

concentrations selectively reduced α1 phosphorylation by approximately 1 P (~0.93 P decrease), while β1 (~0.18 P decrease) and γ1 levels (decrease within error) remained relatively stable (Fig. 3b). Even at high PP1A concentrations, substantial phosphorylation persisted, indicating that PP1A selectively removes the activating phosphorylation at T183 on the α1 subunit, whereas autophosphorylation sites appear protected from dephosphorylation. This asymmetric dephosphorylation control underscores that autophosphorylation modifications are kinetically stable once established, potentially persisting beyond acute signaling events (Fig. 3c).

Site-directed mutagenesis defines CaMKK2 specificity

To distinguish CaMKK2-driven phosphorylation from AMPK autophosphorylation, we generated two α1-subunit mutants that selectively disrupt different aspects of AMPK activation (Fig. 3d, Fig. S3a). The α1-T183A mutant prevents activation loop phosphorylation, blocking canonical activation. The α1-K56N mutant disrupts ATP binding, abolishing all kinase activity; thus, any phosphorylation detected must originate from an external kinase. This dual-mutant strategy allows us to definitively separate upstream kinase targets from downstream autophosphorylation events.

RPLC-MS analysis revealed striking differences in CaMKK2-mediated modification patterns (Fig. 3e). Wild-type AMPK exhibited phosphorylation levels (α1: 4.44 ± 0.03P, β1: 2.34 ± 0.01P, γ1: 0.46 ± 0.01P) consistent with previous experiments. The α1-T183A mutant showed virtually no detectable phosphorylation on any subunit, indicating that without T183 phosphorylation, the activation loop cannot open and no autophosphorylation cascade can proceed. Most revealing was the catalytically inactive K56N mutant, which acquired exactly one phosphorylation on α1 and none on β1 (Fig. S3b). Since T183A prevents all phosphorylation, this single modification in K56N demonstrates that T183 is the sole direct CaMKK2 target with all other phosphorylation sites across the α1, β1, and γ1 subunits being generated exclusively through AMPK autophosphorylation following this initial activating event.

Allosteric activation bypasses canonical phosphorylation requirements

AMPK harbors an allosteric drug and metabolite (ADaM) binding site at the α-kinase domain and β-subunit interface, activated by small molecules up to 10-fold[44]. We employed PF-739, a small molecule ADaM site activator, demonstrating dose-dependent AMPK activation with 3.8-fold enhancement over AMP alone (Fig. 3g-i).[45]

We next assessed whether allosteric stimulation alone could initiate the phosphorylation cascade in the absence of the canonical upstream trigger. While AMP alone produced minimal phosphorylation in both wild-type and T183A AMPK, addition of PF-739 resulted in substantial and nearly identical phosphorylation levels in both variants (WT: α1: 4.79 ± 0.12P, β1: 1.79 ± 0.01P; T183A: α1: 4.63 ± 0.12P, β1: 1.79 ± 0.01P) (Fig. 3j, Extended Data Fig. S3c-d). These phosphorylation levels are comparable to those achieved through CaMKK2 activation, demonstrating that allosteric activation enables robust autophosphorylation even when T183 cannot be phosphorylated. This establishes that activation loop phosphorylation is not strictly required for AMPK to execute its regulatory phosphorylation program. These results support a model where PF-739 binding promotes a catalytically competent conformation that bypasses the canonical requirement for activation loop phosphorylation, establishing dual entry points into the activation cascade that enable distinct activation pathways to converge on a autophosphorylation cascade (Fig. 3k, Fig. S4a)[46].

Site-specific phosphorylation kinetics reveal mechanistic hierarchy

To identify specific sites causing the observed phosphorylation hierarchy, we employed bottom-up MS using identical aliquots from the CaMKK2-AMPK reaction samples (Fig. 4a, Fig. S5b-d). Phosphorylation kinetics were quantified by monitoring extracted ion chromatograms (EIC) for peptide pairs showing inversely correlating behavior (Fig. 4b-c, Table S3-5, Fig. S5a). Sixteen peptide pairs generated kinetic profiles from unphosphorylated peptide disappearance, providing the most reliable measure of modification progression (Fig. 4d).

Our analysis revealed striking differences in phosphorylation rates and extents across AMPK sites (Fig. 4e-f). The most rapid autophosphorylation occurred at α1-S496, an inhibitory site[47], exhibiting exceptionally high kinetic rate (0.16 ± 0.05 min^{-1}). This reflects efficient trans-autophosphorylation where CaMKK2-activated AMPK molecules phosphorylate S496 on neighboring complexes faster than CaMKK2 phosphorylates α1-T183 (0.077 ± 0.005 min^{-1}).

The well-characterized β1-S108 showed excellent kinetic behavior (R^2 = 0.99) with complete modification by 50 minutes[46]. β1-T148, crucial for glycogen binding[48], exhibited higher rate constant (0.077 ± 0.083 min^{-1}) but moderate extent (0.45) and quantification challenges from complex peptide sequence, making kinetic parameter interpretation less reliable[48]. This kinetic analysis established distinct rate categories, enabling discrimination between rapid primary regulatory events and slower secondary modifications.

Several sites displayed moderate kinetics, including α1-S176 (0.053 ± 0.014 min^{-1}, extent = 0.62) and γ1-S9 (0.055 ± 0.027 min^{-1}, extent = 0.80), while sites like α1-T388 (0.007 ± 0.004 min^{-1}, extent = 0.35) showed very slow kinetics likely representing secondary regulatory mechanisms.

Among the analytical challenges was quantification of convoluted phosphorylations at the α1 C-terminal regulatory domain. However, a shorter 23-residue peptide from semi-specific trypsin cleavage (SSEVSLTSSVTSLDSSPVDLTPR/P) separated into three distinct chromatographic peaks corresponding to phosphorylation at α1-S516, α1-S524, and α1-T526 (Fig. S5e). The unphosphorylated peptide decreased slowly (k = 0.008 ± 0.008 min^{-1}) but achieved high phosphorylation extent (0.81). The total phosphorylation is distributed across three sites with chromatographic peak area ratios (S516 : S524 : T526 = 1.0 : 1.9 : 0.7) indicating preferential S524 modification.

The α1 and β1 subunit difference between peptide-level and intact protein quantification (4.6P vs. 5.3P, 2.0P vs. 2.7P, respectively) suggests the presence of modifications not captured by bottom-up analysis. These discrepancies, rather than

representing limitations, highlight the necessity of direct proteoform characterization to definitively identify modification combinations that remain masked in peptide-based approaches.

Our site-specific kinetic analysis provides detailed mechanistic insight, revealing that AMPK autophosphorylation involves a complex hierarchical organization of sites with distinct kinetic properties. However, while bottom-up analysis identified individual phosphorylation sites, the specific combinations of modifications within intact proteoforms remained unresolved.

Top-down sequencing validates proteoform architecture

To characterize proteoform architecture and validate quantitative measurements, we employed ultrahigh resolution (>400,000 at 400 *m/z*) MS top-down sequencing analysis. Direct Nano-ESI of denatured AMPK subunits yielded high-quality spectra with isotopic resolution. However, the α1 subunit showed strong signal suppression due to size-related effects and was only detectable in the unphosphorylated control sample. In contrast, the smaller β1 and γ1 subunits dominated the signal response in both conditions (Fig. 5a, Fig. S6a-b).

Examination of β1 intact mass spectra from the CaMKK2-treated sample revealed heterogeneous phosphorylated species (1P-7P), with doubly phosphorylated (2P) as the major component (Fig. 5b). Top-down measurements showed total β1 phosphorylation of 3.1P, slightly higher than our earlier RPLC-TOF analysis (2.7P), likely due to different ionization conditions. Summing phosphorylation extents from all identified peptides in bottom-up analysis yielded only 2.0P, revealing a 0.7-1.1P discrepancy compared to intact protein measurements. This missing phosphorylation made the predominant 2P β1 ideal for structural characterization to identify undetected modification sites. Quadrupole isolation of the 2P β1 23+ precursor (1323 *m/z*) achieved mass species selectivity with high mass accuracy (1.9 ppm) (Fig. 5c-d).

Comprehensive structural characterization was performed using complementary fragmentation approaches combining collision-induced dissociation (CID) and electron capture dissociation (ECD) at optimized parameters (Fig. 5e, Fig. S7). Data processing used in-house

MASH software with manual curation.[49] The combined fragmentation experiments yielded 179 high-confidence fragment ions (43 *b*-, 54 *c*-, 34 *y*-, 48 *z*-type) across the 269-residue β1 sequence, achieving 54% backbone coverage and high mass precision (Figure 5f-g). Systematic fragment analysis revealed the major β1 bis-phosphorylated proteoform (2P) carries phosphorylation at S24/25 and S108.

The first phosphorylation was localized to the S24/25 double serine motif based on c22, c23, and c24 fragment ions, with predominant modification at S24 (Fig. S8), consistent with the mutually exclusive phosphorylation pattern described for this site.[39] The identification of S24/25 phosphorylation directly addresses the quantitative discrepancy between intact protein and peptide-level measurements. This site was absent from bottom-up analysis due to poor N-terminal coverage; the 6-residue tryptic peptide DSSGTK containing S24/S25 was not detected.

The second phosphorylation site, S108, was definitively assigned based on 27 high-confidence fragment ions spanning this region. This S24/25+S108 combination represents a notable finding, as S24/25 phosphorylation has been linked to extranuclear distribution, while S108 phosphorylation facilitates allosteric activation by stabilizing the ADaM site binding pocket[37,50]. The strong predominance of the 2P species in intact mass spectra, combined with the consistent identification of this specific S24/25+S108 combination, suggests a channeled proteoform formation pathway rather than stochastic modification of available sites. Notably, β1-S101 and β1-T148 phosphorylation could not be detected in our top-down analysis, despite identification in bottom-up experiments, indicating these represent minor proteoforms under these experimental conditions. Our ultra-high-resolution MS analysis thus provides definitive structural validation of complex AMPK proteoform architectures.

Mechanistic model and site-level mapping of AMPK phospho-proteoforms

Our comprehensive analysis creates a model for AMPK proteoform regulation based on four key mechanisms (Fig. 6a): (1) Dual entry into the activation cascade through CaMKK2-dependent α1-T183 phosphorylation or allosteric activation. (2) Hierarchical phosphorylation

kinetics with defined priorities, where α1-S496 shows highest modification efficiency. (3) Channeled proteoforms with selective co-occurrence, exemplified by the predominant β1-S24/25 + S108 combination coupling localization and allosteric sensitivity. (4) Asymmetric dephosphorylation control where PP1A reverses α1-T183 but not autophosphorylation sites, enabling proteoform persistence beyond acute signaling.

Our structural analysis revealed that identified phosphorylation sites cluster into four distinct hotspots (Fig. 6b-c). The activation sites and catalytic center (Fig. 6d) cluster α1-T183, α1-S176, and β1-S108, where α1-T183 and β1-S108 drive main and allosteric activation. The α1 ST-loop (Fig. 6e) encompasses S496, S524, S516, and T526, orchestrating negative feedback through electrostatic interactions[47,51]. The α1-auto-inhibitory domain and α-hook region (Fig. 6f) contain phosphorylations at T388, S397, S360, S356, and T355[52]. The β1 carbohydrate-binding module (Fig. 6g) features T148 mediating glycogen sequestration[48], alongside S96 and S101. This spatial organization reveals how AMPK integrates multiple regulatory inputs through autophosphorylation cascades that create proteoform diversity, extending beyond a binary activation model to enable fine-tuned kinase activity and function.

DISCUSSION

Protein phosphorylation generates functionally distinct proteoforms through complex, multisite modification cascades, yet resolving their temporal dynamics and combinatorial patterns remains a major analytical challenge. Conventional MS approaches capture either peptide-level kinetics[13,15,16] or intact protein states[17–19], but rarely both with sufficient resolution to link modifications to regulatory architectures. By unifying intact-mass profiling, site-specific kinetics, and top-down sequencing, our platform reveals when sites are modified, how events propagate, and which combinations form co-occurring proteoforms.

Applied to AMPK, this strategy expands the classical activation model centered on α1-T183 phosphorylation[22,28]. Intact-mass measurements uncovered subunit-specific hierarchies demonstrating that extensive autophosphorylation is triggered by a single CaMKK2-initiated priming event. Kinetic profiling resolved distinct temporal classes: rapid modification of α1-

S496, moderate rates at allosteric control sites[31], and slow modifications clustered in regulatory domains. These findings reveal for the first time the hierarchical ordering during activation. Phosphatase experiments revealed asymmetric regulation where PP1A selectively removes activation-loop phosphorylation while leaving autophosphorylation sites intact. While prior studies observed one autophosphorylated site corresponding to α1-S496 being resistant to protein phosphatases using western blot[39], our intact protein measurements demonstrate that specific deactivation does not roll back the proteoform diversity generated through activation.

Allosteric stimulation revealed a second activation route. PF-739 initiated robust autophosphorylation without T183 phosphorylation. Although allosteric activation without T183 phosphorylation may have limited physiological relevance for canonical AMPK function[46], the substantial proteoform remodeling suggests diverse modification states can be generated through alternative pathways. Top-down sequencing confirmed the dominant β1 bis-phosphorylated proteoform (S24/25 + S108), validating intact-mass assignments and revealing channeled pathways coupling localization and allosteric sites[37,48].

Coherence across datasets validates our approach. Sites missed in bottom-up workflows were recovered by intact and top-down analysis, while discrepancies exposed biases obscuring regulatory logic. However, our in vitro measurements do not capture cellular context: in vivo proteoform distributions will depend on cell type, subcellular localization, metabolic state, and local kinase and phosphatase concentrations[23].

In summary, our findings establish a proteoform-centric view of multisite kinase regulation, revealing how dynamic modification hierarchies and coordinated phosphorylation pathways shape functional states. By integrating intact-mass profiling, site-specific kinetics, and top-down sequencing, this platform resolves resolves temporal and combinatorial phosphorylation relationships inaccessible to any single method. More broadly, this platform provides a generalizable framework for characterizing therapeutic kinase targets where proteoform-specific regulation remains poorly understood, demonstrating that proteoform-resolved analysis is critical for understanding kinase regulatory dynamics.

METHODS

Genes and Protein Constructs

Recombinant protein sequences were based on UniProt entries human AMPK alpha1 (Q13131), beta1 (Q9Y478), and gamma1 (P54619). The expression plasmid pET28-H6-AMPKγ1β1α1 for AMPK full-length, with His tag (MSYYHHHHHHEGVRTM-) N-terminally fused to the alpha subunit, and pET24 H6GST-hPP1Aα (aa1-314, PP1A domain) was generated by Karsten Melcher Lab and kindly provided by Van Andel Institute. Site-directed mutations on AMPK α K56N and T183A were introduced using the Q5 site-directed mutagenesis kit (New England Biolabs) and confirmed using long-read DNA sequencing (UW-Madison Biotechnology Center).

Expression and Purification

AMPK and PP1Aα were produced as recombinant proteins in One Shot BL21 Star (DE3) E. coli (Thermo Fisher). Cells were grown in 1 L baffled flasks to OD_{600} = 0.8-1.0, induced with 0.1 M Isopropyl β-D-1-thiogalactopyranoside and continued at 18 °C for 20 h. Cell pellets were lysed in His equilibration buffer (20 mM imidazole, 40 mM phosphate, 300 mM NaCl, pH 8) by sonication. His-tagged proteins were purified using HisPur Ni-NTA resin (Thermo Fisher) with sequential washes (50 mM imidazole) and elution (300 mM imidazole). Proteins were buffer-exchanged into storage buffer (20 mM phosphate, 150 mM NaCl, 300 mM imidazole, 15% glycerol, 2 mM DTT), concentrated to 5-10 mg/mL, and stored at -80 °C. Concentrations were determined by Bradford assay (BioRad) or NanoDrop (Thermo Scientific). CaMKK2 (CaMKK beta isoform 2 [1 – 541]) was obtained through the MRC PPU Reagents and Services facility (MRC PPU, College of Life Sciences, University of Dundee, Scotland):

AMPK Phosphorylation Reactions

All reactions were performed in assay buffer (50 mM HEPES, 100 mM NaCl, 2 mM DTT, 0.01% Brij 35). CaMKK2 was premixed with calmodulin (Enzo Life Sciences) at a 1:2 molar ratio. For phosphorylation, 7.5 μM AMPK was incubated with 0.155 μM CaMKK2 and 0.31 μM calmodulin in the presence of 500 μM ATP, 200 μM AMP, 5 mM $(CH_3COO)_2Mg$, and 1 mM

$CaCl_2$ at 20 °C for up to 200 min in [240 µL total volume]. Aliquots (~15 µg protein) were quenched at defined intervals with 0.1% formic acid (FA). For concentration-dependent PP1A phosphatase experiments, PP1A was added at varying concentrations to CaMKK2 AMPK mixtures, and samples were quenched after 200 min.

Quenched reactions were desalted using chloroform-methanol-water precipitation. AMPK was diluted into 400 µL water, precipitated with 400 µL methanol, phase-separated with 100 µL chloroform, and centrifuged at 15,000 g for 10 min. Following supernatant removal, 400 µL methanol was added and mixed by rocking. After centrifugation, proteins were further desalted by two consecutive methanol washes. Air-dried pellets were stored at -80°C until analysis.

Intact LC-MS Analysis

Desalted reaction samples were reconstituted in 5% FA/20% acetonitrile-isopropanol and adjusted to 200 ng/µL. LC-MS was performed using nanoAcquity UPLC (Waters) coupled to Impact II Quadrupole Time-Of-Flight (QTOF) (Bruker Daltonics). Samples (300-500 ng) were separated on a home-packed C4 column (Halo, 2.7-µm, 250-µm ID, 10 cm, 1,000 Å) using gradient: 0-3 min, 10% B; 3-20 min, 10-80% B; 20-24 min, 80-95% B; 24-30 min, 95%-10% B (A: 0.1% FA in H_2O; B: 0.1% FA in acetonitrile) at 4 µL/min.

Mass spectra were acquired at 0.5 Hz over 300-3000 m/z. Source parameters: capillary voltage 4500 V, nebulizer pressure 0.5 bar, dry gas 4.0 L/min at 200°C. Ion transfer settings: funnel RF 300 V, quadrupole energy 5 V, low mass cutoff 650 m/z, isCID 10 V, collision RF 2600 Vpp.

Data processing used Compass Data Analysis (Bruker). Summed mass spectra were generated from fixed time windows. Deconvolution employed MaxEnt with different parameters for isotopic resolved (β/γ: resolution 40,000) versus non-resolved (α: resolution 10,000) charge envelopes. Spectra were smoothed (Savitzky-Golay 0.2), background subtracted (0.55), and peak-picked. Peak lists were manually curated for phosphorylation masses and exported for

weighted average calculations. The total weighted phosphorylation average was calculated by the following formula:

$$\frac{(P0*0+P1*1+\cdots* Pi*i)}{(P0 + P1 + ... + Pi)} = p_{total}$$

Bottom-up MS Analysis

Desalted reaction samples were reconstituted and neutralized with ammonium bicarbonate (pH 8), before being reduced with 10 mM TCEP (37°C, 30 min), alkylated with 500 mM chloroacetamide (RT, 30 min), and digested with trypsin (37°C, overnight). Peptides were desalted using C18 stage tips and analyzed by LC-MS/MS.

Samples (200 ng) were separated on Ion Optics columns (25 cm × 75 µm, C18 1.6 µm) at 55°C using 50 min gradients (2-37% B, then 37-85% B over 5 min; A: 0.2% FA in water, B: 0.2% FA in ACN) at 400 nL/min. Analysis used a Trapped Ion Mobility Spectrometry (tims)-TOF Pro (Bruker) in PASEF mode with ion mobility 0.60-1.60 Vs/cm² and standard fragmentation parameters (10 MS/MS scans, 1.17 s cycle time, 20-59 eV collision energy).

Data were processed in Skyline (v23.1.0.380) to extract peak areas (area under the curve, AUC) from corresponding phosphorylated/unphosphorylated peptide pairs. Peak areas were normalized to the maximum value within each peptide series and analyzed in GraphPad Prism. Unphosphorylated peptides were fit to one-phase decay models to obtain rate constants (k, min^{-1}), while phosphorylated peptides were fit to one-phase association models for validation. Phosphorylation extent was calculated as $(AUC_{max} - AUC_{min})/AUC_{max}$ from the normalized peak areas, representing the fraction of peptide phosphorylated. Only peptide pairs showing inverse correlation were included in the final analysis.

Phosphorylation kinetics were determined from unphosphorylated peptide disappearance (normalized to initial values), as this provides the most reliable measure of modification progression independent of differential ionization efficiencies between modified and unmodified forms.

Top-down MS

Phosphorylated AMPK samples were analyzed using solariX XR 12T Fourier-Transform Ion Cyclotron Resonance (FTICR) mass spectrometer (Bruker) coupled to TriVersa Nanomate (Advion). NanoESI conditions: 0.45 PSI desolvating gas pressure, 1.5-1.55 kV voltage, 3 L/min dry gas at 180 °C. Source optics were optimized: capillary exit 240 V, detector plate 220 V, funnel 1 at 150 V, skimmer 50 V, funnel RF 300 Vpp, octopole frequency 5 MHz with 600 Vpp RF, collision cell at 2 MHz with 2000 Vpp RF.

Mass spectra were acquired with 2M data points over 200-4000 m/z range. Precursor isolation used ≥4 m/z windows. Collision-activated dissociation (CAD) employed 12-35 V collision energy. Electron capture dissociation (ECD) parameters: pulse length 0.01-0.03 s, bias 0.5-1.5 V, lens voltage 5-15 V. Fragment ion assignments were performed using standard top-down proteomics approaches for proteoform characterization. MS2 data were analyzed using MASH Native for proteoform sequencing and PTM localization[49]. Fragments were identified using eTHRASH algorithm. All fragments were manually validated.

Data Integration and Analysis

Intact protein phosphorylation levels were quantified from deconvoluted mass spectra using weighted averages. Site-specific extent from bottom-up analysis were correlated with total phosphorylation measurements. FTICR MS2 data provided definitive proteoform identification and phosphosite localization and used for complementing the results.

ACKNOWLEDGEMENTS

B.K. was supported by the European Union grant 101068151, Top-AMPK, HORIZON-MSCA-2021-PF-01. B.K. thanks Mel Park for co-supervising the Top-AMPK project. H.T.R. would like to acknowledge support from the National Heart, Lung, and Blood Institute of the NIH under Award Number T32HL007936 through the UW-Madison Cardiovascular Research Center and the Ruth L. Kirschstein NRSA Individual Predoctoral Fellowship under Award Number F31HL178305. C.U. would like to acknowledge funding from the ARIADNE VIBE project, Grant

Agreement No. 964553. Y.G. would like to acknowledge NIH R01HL109810, R01GM117058, and S10 OD018475 (to Y.G). The author(s) thank the University of Wisconsin Carbone Cancer Center Cancer Informatics Shared Resource, supported by P30 CA014520 for use of its services. All mass spectrometry data reported in this study were acquired at the University of Wisconsin–Madison Human Proteomics Program Mass Spectrometry Facility. We thank Dr. Yanlong Zhu, the facility manager, for expert instrument support and assistance.

AUTHOR CONTRIBUTIONS

Y.G. conceived the study. B.K., C.U., and Y.G. designed the experiments; Y.G. supervised the experimental work; B.K., L.B. expressed and purified proteins; B.K. and H-J.C. established and performed phosphorylation assays and MS sample preparation under Y.G.'s direction; H-J.C. acquired FTICR top-down MS fragmentation data; B.K., H.T.R and Z.G. acquired Impact II top-down MS intact data; B.K. and H-J.C. acquired timsTOF bottom-up data; B.K. and H-J.C. analyzed and visualized MS data; B.K. and M.W. performed kinase activity assays; B.K. and S.J.M. calculated total phosphorylation and charge state distribution. Y.G. and C.U. supervised the project; B.K., H-J.C, C.U. and Y.G. evaluated results; B.K., H-J.C, C.U. and Y.G. wrote the paper with comments from other co-authors.

CONFLICT OF INTEREST

The authors declare no competing financial interests or conflicts of interest in relation to the work described in this manuscript.

FIGURES AND CAPTIONS

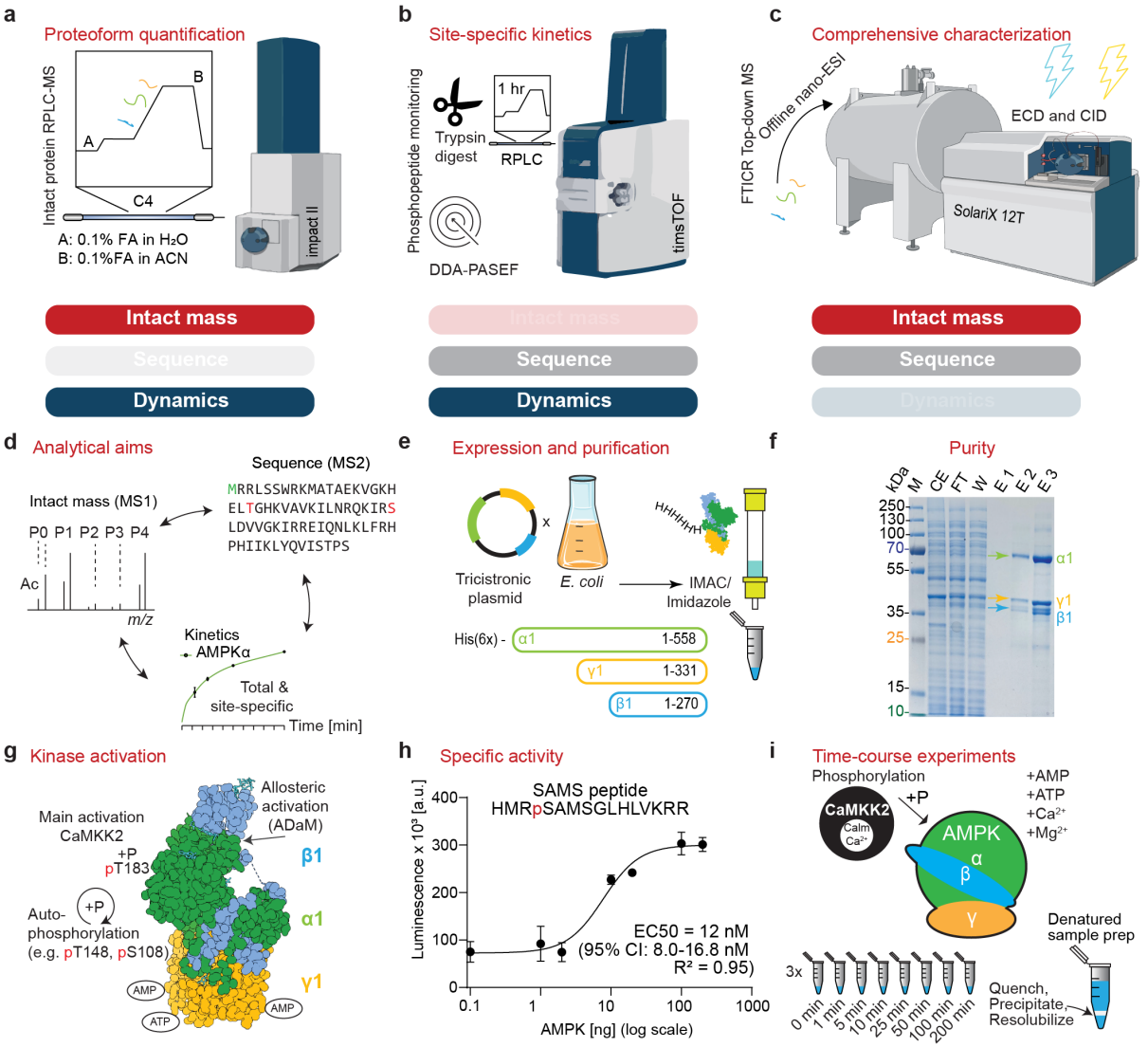

Figure 1: Hybrid precision mass spectrometry (MS)-strategy for resolving kinase phosphorylation dynamics. (a) Intact proteoform tracking via LC-MS. **(b)** Site-specific phosphorylation kinetics via bottom-up MS. **(c)** Top-down proteoform characterization using ultra high-resolution MS with various fragmentation options. **(d)** Conceptual integration of the three approaches to capture intact mass, sequence information, and temporal dynamics. **(e)** Heterologous AMPK expression and affinity purification workflow. **(f)** SDS-PAGE analysis confirming purity of affinity purified AMPK complex with approximately stoichiometric subunit ratios. **(g)** AMPK activation mechanism: AMP binding enhances CaMKK2-mediated T183 phosphorylation and subsequent autophosphorylation cascade. **(h)** Dose-response curve showing AMPK enzyme titration with SAMS peptide substrate. X-axis shows total AMPK amount added to 5 µL reactions on logarithmic scale. **(i)** Time-course phosphorylation workflow: AMPK incubated with CaMKK2 and cofactors, with samples quenched at defined intervals and prepared by chloroform-methanol-water-precipitation.

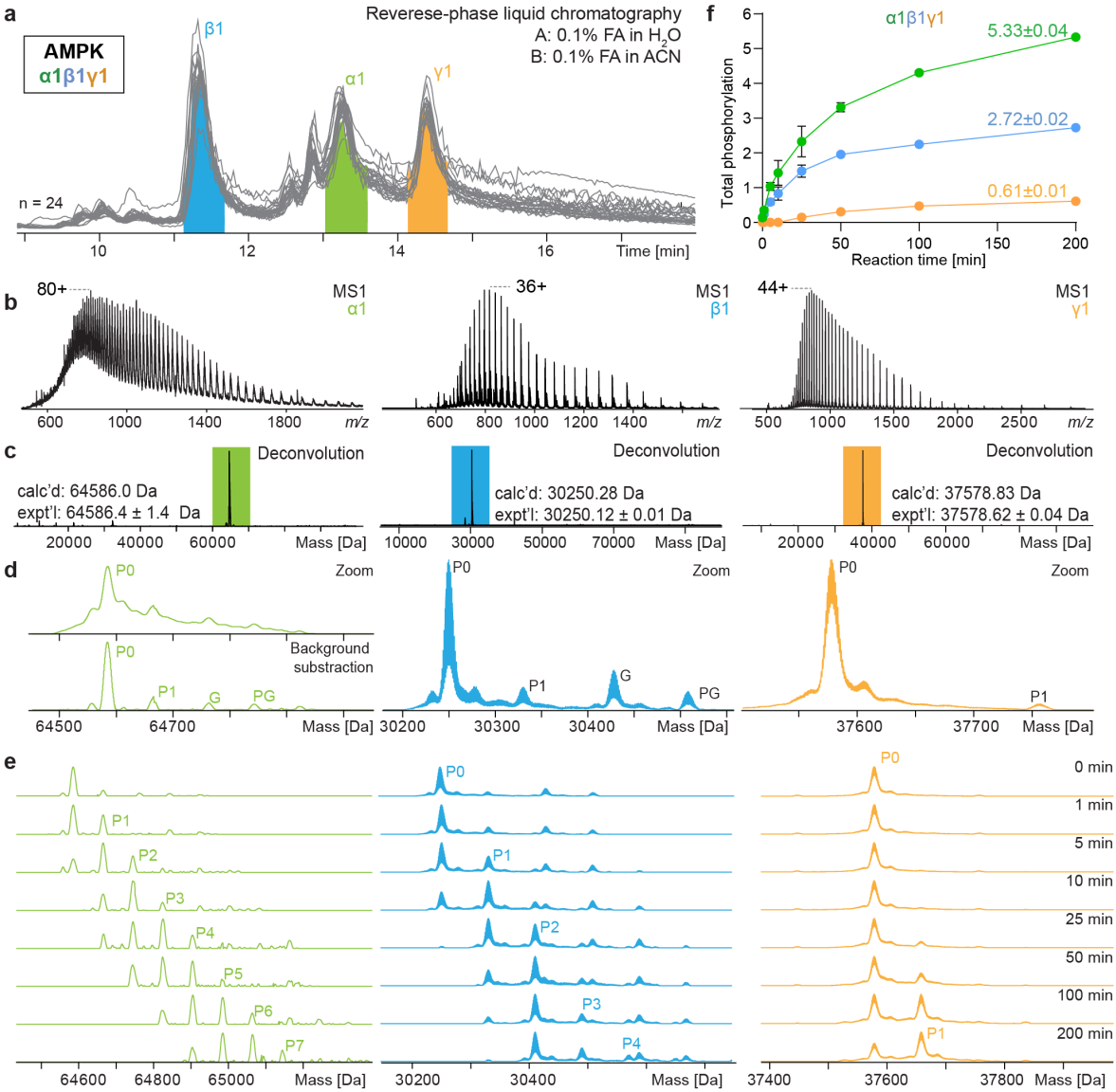

Figure 2: AMPK proteoform quantification by intact protein RPLC-MS during CaMKK2-mediated activation. (a) Total ion chromatograms of 24 consecutive runs across the phosphorylation time course. **(b)** MS1 intact protein spectra at 0 min reaction time with most abundant charge states labeled. **(c)** Deconvoluted mass spectra for proteoform identification showing calculated (calc'd) and experimental (expt'l) masses. **(d)** Quantifiable peaks labeled with their corresponding proteoforms. P = Phosphorylation, G = Gluconoylation, PG = Phosphogluconoylation. **(e)** Representative deconvoluted mass spectra showing temporal progression of mass increases corresponding to sequential phosphorylation events. **(f)** Temporal changes in total phosphorylation for each AMPK subunit over 200 min (mean ± SEM, n = 3).

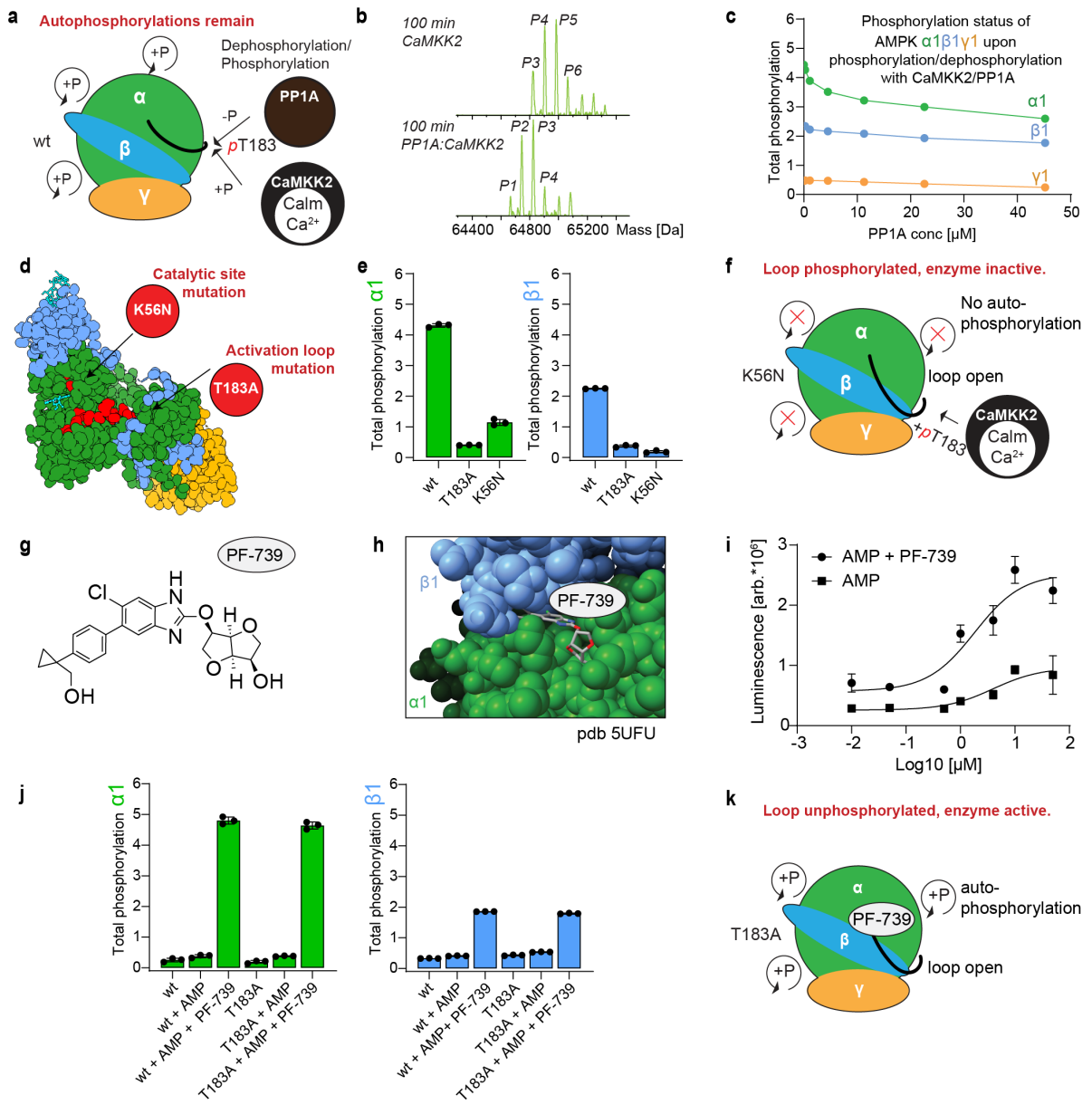

Figure 3: Deciphering canonical and allosteric mechanisms of AMPK activation. (a) Schematic showing the competitive phosphorylation-dephosphorylation reactions: CaMKK2-mediated phosphorylation versus PP1A-mediated dephosphorylation of AMPK. **(b)** MS1 intact protein spectra of CaMKK2-phosphorylated AMPK demonstrating that total α1 phosphorylation decreases (~1P) upon phosphatase (PP1A) addition. **(c)** Concentration-dependent phosphorylation-dephosphorylation dynamics showing that α1 decreases earlier and more substantially than β1 and γ1 subunits (mean ± SEM, n=3). **(d)** Structural model showing site-directed mutations: catalytic site (K56N) and activation loop (T183A). **(e)** Total phosphorylation quantification in WT and mutants following CaMKK2 treatment (mean ± SEM, *n=3*), T183A is inactive upon CaMKK2 addition while K56N increases selectively (~1 P) in α1 subunit. **(f)** Schematic model illustrating CaMKK2-mediated activation loop phosphorylation as the sole direct target in catalytically inactive K56N mutant. **(g-h)** PF-739 structure and ADaM site binding location. **(i)** ADP-Glo kinase assay showing dose-dependent allosteric activation (arbitrary units, mean ± SEM, *n=3*). Peak activation showing 3.8-fold enhancement over AMP alone. **(j)** Phosphorylation analysis of WT and T183A AMPK following allosteric activation; wt and T183A show intense phosphorylation by allosteric activation, indicating that the T183 phosphorylation is circumvented. **(k)** Proposed mechanistic model illustrating PF-739-

mediated enzyme activation despite unphosphorylated activation loop, establishing dual entry into the autophosphorylation cascade.

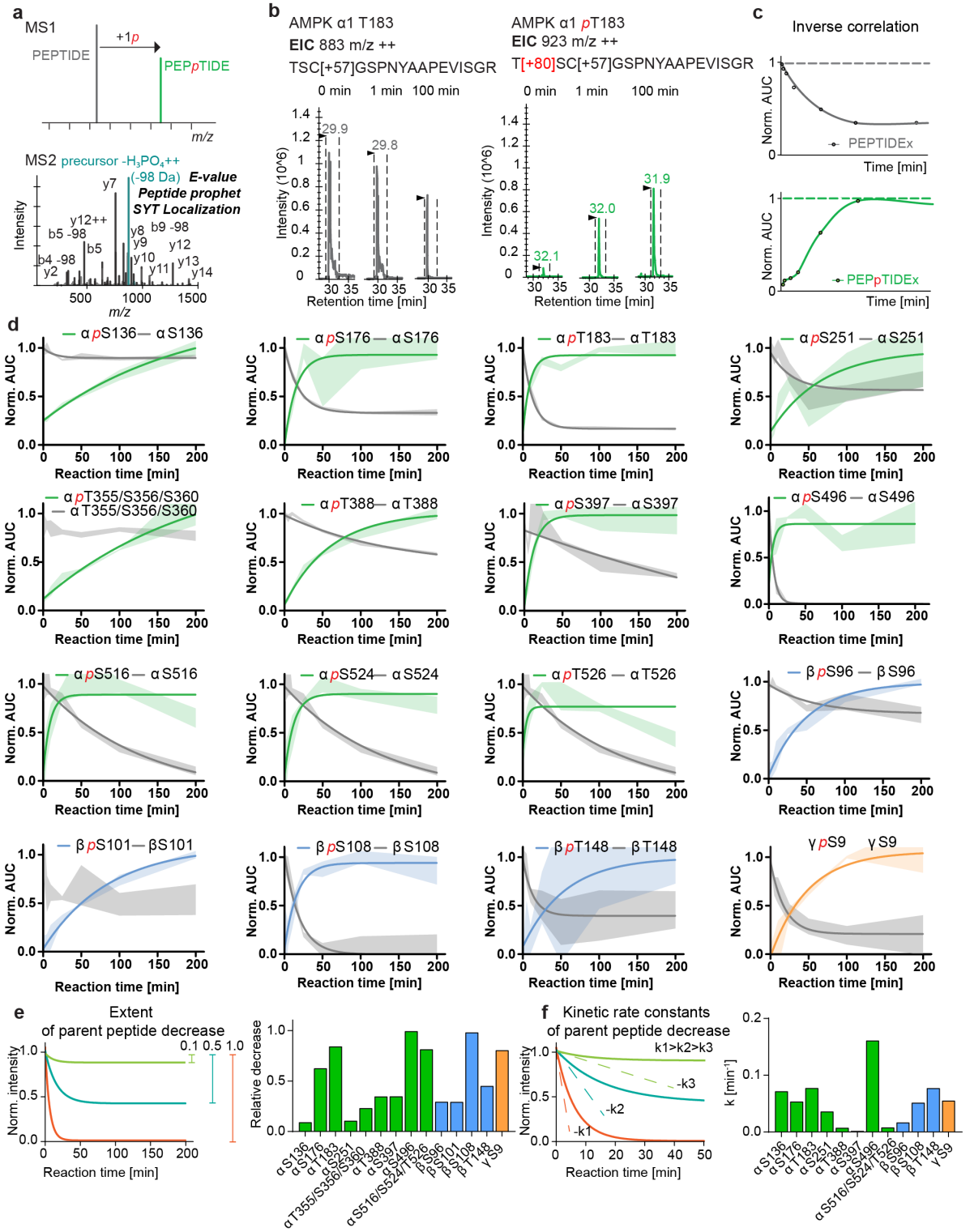

Figure 4: Site-specific phosphorylation kinetics reveal mechanistic hierarchy using bottom-up MS. (a) MS1 **of** phosphorylated/unphosphorylated peptide pair tracking and MS2 spectrum showing spectral quality and phosphopeptide identification. **(b)** Temporal progression at 0, 1, and 100 min for parent peptide and phosphopeptide T183 showing inversely correlating intensities. **(c)** Schematic of kinetic plots with inversely correlating changes over time monitored as Normalized Area Under Curve (AUC). **(d)** Site-specific phosphorylation kinetics for 16 peptide pairs with color-coded subunit assignment (α1: green, β1: blue, γ1: yellow-orange). One-phase decay curve fitting applied. Shaded bands represent mean ± SEM. **Note**: S516, S524 and T526 have the same parent peptide. Parent peptides of

α1 T355/T356/S360 and β1 S101 could not be fit with the one-phase decay model. **(e)** Schematic showing how extents of phosphorylation were determined from parent peptide decrease; bar graph showing extents of phosphorylation. **(f)** Schematic showing how kinetic rate constants (k) were obtained by fitting peptide disappearance curves to a one-phase decay model. **Note**: Parent peptides for β1 S101 and α1 S397 showed early-timepoint variability within the first 10 min, could not be fit to the one-phase decay model and were only analyzed for their extent. The α1 S397 quantification challenges likely arise from (1) the peptide containing one missed cleavage site, complicating accurate quantification, and (2) sequence overlap with the T388-containing peptide, where T388 phosphorylation also decreases the S397 parent peptide intensity.

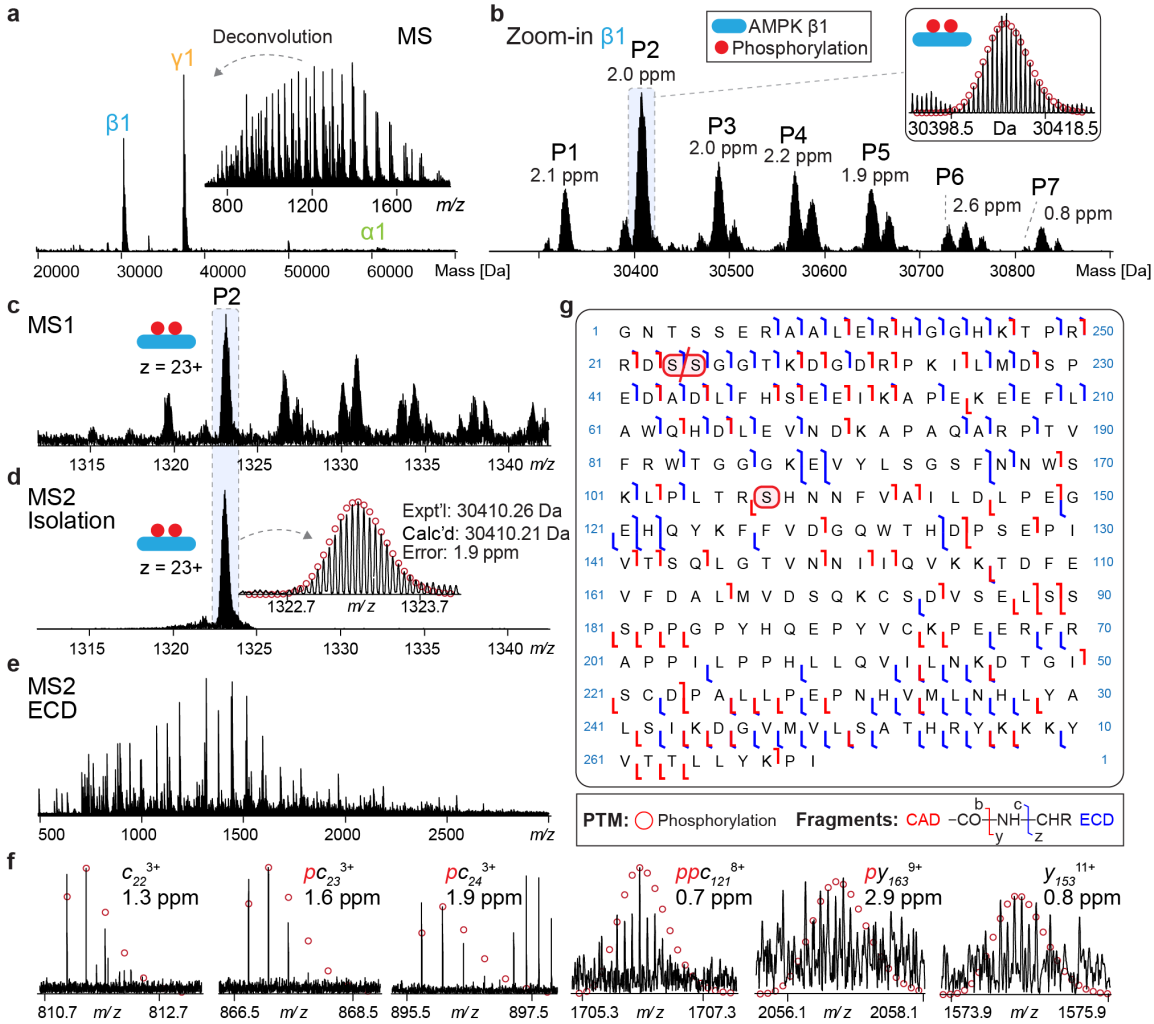

Figure 5: Top-down sequencing identifies doubly phosphorylated AMPK β1 proteoform architecture. (a) Deconvoluted mass spectrum of denatured AMPK subunits with raw mass spectrum shown in inset. **(b)** Zoom-in shows isotopically resolved β1 phosphorylation states (1P-7P) with 2P as the most abundant species. **(c)** The 23+ charge state of the β1 shows a peak distribution similar to the deconvoluted spectrum in (b). **(d)** Quadrupole isolation of 2P β1 23+ precursor ion (1323 *m/z*) with isotopically resolved peak inset. **(e)** Representative ECD fragmentation spectrum showing extensive fragmentation pattern. **(f)** Selected fragment spectra (*p*: singly phosphorylated; *pp*: doubly phosphorylated). Mass errors are reported, and isotopic fittings are shown in red circles. Shift from fragment pattern c_{22}, c_{23}, c_{24} versus assigned positions *p*S24, *p*S25 due to N-terminal glycine cleavage. **(g)** Combined fragment map from complementary CID and ECD experiments. Fragment notation: hook direction indicates type, color denotes method (blue: ECD, red: CID).

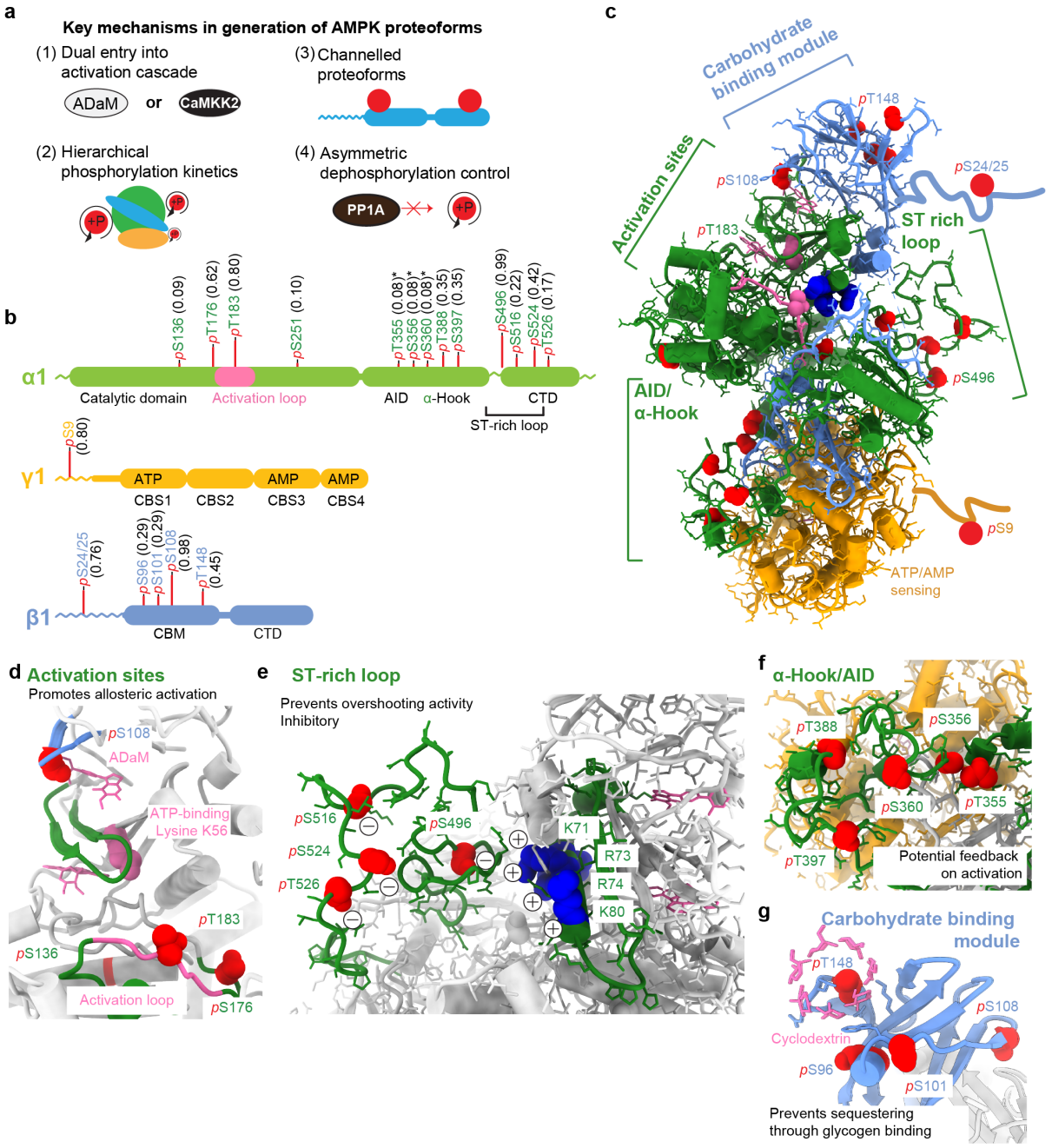

Figure 6. Spatial organization and regulatory mechanisms of AMPK phosphorylation sites revealed by integrated proteoform analysis. (a) Summary of mechanisms contributing to AMPK proteoform diversity. **(b)** Domain organization of AMPK α1β1γ1 subunit isoforms showing main functional domains and positions of identified phosphorylation sites. Red bar heights reflect relative extent of phosphorylation determined from kinetic analysis. Four CBS domains with nucleotide binding pockets here depicted in occupational state of activated enzyme. C-terminal domain (CTD). *Asterisked sites were co-identified on the same peptide and assigned equal phosphorylation stoichiometry. **(c)** AMPK α1β1γ1 protein structure homology model (Swiss-Model) based on PDB 5EZV and 4RER. Disordered termini represented as lines. Red spheres indicate identified phosphorylation sites clustered into four distinct structural hotspots. **(d)** Activation sites and catalytic center hotspot. Phosphorylations proximal to activation sites have critical regulatory functions. **(e)** ST-rich loop hotspot. Phosphorylation sites within this regulatory disordered region create electrostatic interactions

with basic residues near the catalytic center, reducing T183 phosphorylation by upstream kinases and preventing activity overshooting through negative feedback. **(f)** Autoinhibitory domain (AID) and α-hook hotspot. This region facilitates allosteric communication between AMP binding at the γ-subunit and kinase domain activation. The identified phosphorylation cluster (T355, S356, S360, T388, S397) may constitute a feedback mechanism modulating AMP sensitivity and allosteric regulation. **(g)** Carbohydrate-binding module (CBM) hotspot. The CBM mediates AMPK sequestration at glycogen matrices. While β1-T148 has been functionally characterized for glycogen binding regulation, *p*S96 and *p*S101 remain uncharacterized but may influence CBM function due to structural proximity.

REFERENCES

1. Keenan, E. K., Zachman, D. K. & Hirschey, M. D. Discovering the landscape of protein modifications. *Mol. Cell* **81**, 1868–1878 (2021).
2. Walsh, C. T. *Posttranslational Modification of Proteins: Expanding Nature's Inventory*. (Roberts and Co. Publ, Englewood, 2006).
3. Smith, L. M. & Kelleher, N. L. Proteoform: a single term describing protein complexity. *Nat. Methods* **10**, 186–187 (2013).
4. Aebersold, R. *et al.* How many human proteoforms are there? *Nat. Chem. Biol.* **14**, 206–214 (2018).
5. Cohen, P. The origins of protein phosphorylation. *Nat. Cell Biol.* **4**, E127–E130 (2002).
6. Humphrey, S. J., James, D. E. & Mann, M. Protein Phosphorylation: A Major Switch Mechanism for Metabolic Regulation. *Trends Endocrinol. Metab.* **26**, 676–687 (2015).
7. Steinberg, G. R. & Carling, D. AMP-activated protein kinase: the current landscape for drug development. *Nat. Rev. Drug Discov.* **18**, 527–551 (2019).
8. Nikolic, I., Leiva, M. & Sabio, G. The role of stress kinases in metabolic disease. *Nat. Rev. Endocrinol.* **16**, 697–716 (2020).
9. Hunter, T. The Age of Crosstalk: Phosphorylation, Ubiquitination, and Beyond. *Mol. Cell* **28**, 730–738 (2007).
10. Melby, J. A. *et al.* Novel Strategies to Address the Challenges in Top-Down Proteomics. *J. Am. Soc. Mass Spectrom.* **32**, 1278–1294 (2021).
11. Morgan, J. A. M. *et al.* Extensive protein pyrophosphorylation revealed in human cell lines. *Nat. Chem. Biol.* **20**, 1305–1316 (2024).
12. Choudhary, C. & Mann, M. Decoding signalling networks by mass spectrometry-based proteomics. *Nat. Rev. Mol. Cell Biol.* **11**, 427–439 (2010).
13. Riley, N. M. & Coon, J. J. Phosphoproteomics in the Age of Rapid and Deep Proteome Profiling. *Anal. Chem.* **88**, 74–94 (2016).
14. Oppermann, F. S. *et al.* Large-scale Proteomics Analysis of the Human Kinome. *Mol. Cell. Proteomics MCP* **8**, 1751–1764 (2009).
15. Villén, J., Beausoleil, S. A., Gerber, S. A. & Gygi, S. P. Large-scale phosphorylation analysis of mouse liver. *Proc. Natl. Acad. Sci.* **104**, 1488–1493 (2007).
16. Humphrey, S. J., Azimifar, S. B. & Mann, M. High-throughput phosphoproteomics reveals in vivo insulin signaling dynamics. *Nat. Biotechnol.* **33**, 990–995 (2015).
17. Roberts, D. S. *et al.* Top-down proteomics. *Nat. Rev. Methods Primer* **4**, 38 (2024).
18. Chen, B. *et al.* Coupling functionalized cobalt ferrite nanoparticle enrichment with online LC/MS/MS for top-down phosphoproteomics. *Chem. Sci.* **8**, 4306–4311 (2017).
19. Ge, Y., Rybakova, I. N., Xu, Q. & Moss, R. L. Top-down high-resolution mass spectrometry of cardiac myosin binding protein C revealed that truncation alters protein phosphorylation state. *Proc. Natl. Acad. Sci.* **106**, 12658–12663 (2009).
20. Tang, Q.-Q. *et al.* Sequential phosphorylation of CCAAT enhancer-binding protein β by MAPK and glycogen synthase kinase 3β is required for adipogenesis. *Proc. Natl. Acad. Sci.* **102**, 9766–9771 (2005).
21. Bilbrough, T., Piemontese, E. & Seitz, O. Dissecting the role of protein phosphorylation: a chemical biology toolbox. *Chem. Soc. Rev.* **51**, 5691–5730 (2022).
22. Steinberg, G. R. & Hardie, D. G. New insights into activation and function of the AMPK. *Nat. Rev. Mol. Cell Biol.* **24**, 255–272 (2023).
23. Trefts, E. & Shaw, R. J. AMPK: restoring metabolic homeostasis over space and time. *Mol. Cell* **81**, 3677–3690 (2021).

24. Ripa, R. *et al.* Refeeding-associated AMPKγ1 complex activity is a hallmark of health and longevity. *Nat. Aging* **3**, 1544–1560 (2023).
25. Steinberg, G. R. & Kemp, B. E. AMPK in Health and Disease. *Physiol. Rev.* **89**, 1025–1078 (2009).
26. Ma, H. *et al.* Aging-associated Alteration in the Cardiac MIF-AMPK Cascade in Response to Ischemic Stress. *Nat. Preced.* 1–1 (2008) doi:10.1038/npre.2008.2466.1.
27. Luptak, I. *et al.* Aberrant activation of AMP-activated protein kinase remodels metabolic network in favor of cardiac glycogen storage. *J. Clin. Invest.* **117**, 1432–1439 (2007).
28. Woods, A. *et al.* Ca2+/calmodulin-dependent protein kinase kinase-β acts upstream of AMP-activated protein kinase in mammalian cells. *Cell Metab.* **2**, 21–33 (2005).
29. Yan, Y. *et al.* Structure of an AMPK complex in an inactive, ATP-bound state. *Science* **373**, 413–419 (2021).
30. Hawley, S. A., Russell, F. M. & Hardie, D. G. AMP-activated protein kinase can be allosterically activated by ADP but AMP remains the key activating ligand. *Biochem. J.* **481**, 587–599 (2024).
31. Ovens, A. J. *et al.* Post-Translational Modifications of the Energy Guardian AMP-Activated Protein Kinase. *Int. J. Mol. Sci.* **22**, 1229 (2021).
32. Ross, F. A., MacKintosh, C. & Hardie, D. G. AMP-activated protein kinase: a cellular energy sensor that comes in 12 flavours. *FEBS J.* **283**, 2987–3001 (2016).
33. Neumann, D., Woods, A., Carling, D., Wallimann, T. & Schlattner, U. Mammalian AMP-activated protein kinase: functional, heterotrimeric complexes by co-expression of subunits in Escherichia coli. *Protein Expr. Purif.* **30**, 230–237 (2003).
34. Davies, S. P., Carling, D. & Hardie, D. G. Tissue distribution of the AMP-activated protein kinase, and lack of activation by cyclic-AMP-dependent protein kinase, studied using a specific and sensitive peptide assay. *Eur. J. Biochem.* **186**, 123–128 (1989).
35. Geoghegan, K. F. *et al.* Spontaneous alpha-N-6-phosphogluconoylation of a 'His tag' in Escherichia coli: the cause of extra mass of 258 or 178 Da in fusion proteins. *Anal. Biochem.* **267**, 169–184 (1999).
36. Tuerk, R. D. *et al.* Tracking and quantification of 32P-labeled phosphopeptides in liquid chromatography matrix-assisted laser desorption/ionization mass spectrometry. *Anal. Biochem.* **390**, 141–148 (2009).
37. Warden, S. M. *et al.* Post-translational modifications of the β-1 subunit of AMP-activated protein kinase affect enzyme activity and cellular localization. (2001).
38. Mitchelhill, K. I. *et al.* Posttranslational Modifications of the 5′-AMP-activated Protein Kinase β1 Subunit*. *J. Biol. Chem.* **272**, 24475–24479 (1997).
39. Woods, A. *et al.* Identification of Phosphorylation Sites in AMP-activated Protein Kinase (AMPK) for Upstream AMPK Kinases and Study of Their Roles by Site-directed Mutagenesis *. *J. Biol. Chem.* **278**, 28434–28442 (2003).
40. Smiles, W. J. *et al.* AMPK phosphosite profiling by label-free mass spectrometry reveals a multitude of mTORC1-regulated substrates. *Npj Metab. Health Dis.* **3**, 8 (2025).
41. Rajamohan, F. *et al.* Escherichia coli expression, purification and characterization of functional full-length recombinant alpha2beta2gamma3 heterotrimeric complex of human AMP-activated protein kinase. *Protein Expr. Purif.* **73**, 189–197 (2010).
42. PhosphoSitePlus: Hornbeck, P.V. et al. PhosphoSitePlus, 2014: mutations, PTMs and recalibrations. Nucleic Acids Res. 43, D512–D520 (2015).
43. Garcia-Haro, L. *et al.* The PP1-R6 protein phosphatase holoenzyme is involved in the glucose-induced dephosphorylation and inactivation of AMP-activated protein kinase, a key regulator of insulin secretion, in MIN6 β cells. *FASEB J.* **24**, 5080–5091 (2010).

44. Gu, X. *et al.* Conformational heterogeneity of the allosteric drug and metabolite (ADaM) site in AMP-activated protein kinase (AMPK). *J. Biol. Chem.* **293**, 16994–17007 (2018).
45. Myers, R. W. *et al.* Systemic pan-AMPK activator MK-8722 improves glucose homeostasis but induces cardiac hypertrophy. *Science* **357**, 507–511 (2017).
46. Aledavood, E. *et al.* Understanding the Mechanism of Direct Activation of AMP-Kinase: Toward a Fine Allosteric Tuning of the Kinase Activity. *J. Chem. Inf. Model.* **59**, 2859–2870 (2019).
47. Hawley, S. A. *et al.* Phosphorylation by Akt within the ST loop of AMPK-α1 down-regulates its activation in tumour cells. *Biochem. J.* **459**, 275–287 (2014).
48. Oligschlaeger, Y. *et al.* The Recruitment of AMP-activated Protein Kinase to Glycogen Is Regulated by Autophosphorylation*. *J. Biol. Chem.* **290**, 11715–11728 (2015).
49. Larson, E. J. *et al.* MASH Native: a unified solution for native top-down proteomics data processing. *Bioinformatics* **39**, btad359 (2023).
50. Desjardins, E. M., Day, E. A., Scott, J. W. & Steinberg, G. R. Sensing of Long-Chain Fatty Acyl-CoA Esters by AMPK. in *Nutrient Sensing in Eukaryotes* (eds Russell, F. M. & Hardie, D. G.) 121–137 (Springer US, New York, NY, 2025). doi:10.1007/978-1-0716-4284-9_6.
51. Pearah, A. *et al.* Blocking AMPKαS496 phosphorylation improves mitochondrial dynamics and hyperglycemia in aging and obesity. *Cell Chem. Biol.* **30**, 1585-1600.e6 (2023).
52. Xiao, B. *et al.* Structural basis of AMPK regulation by small molecule activators. *Nat. Commun.* **4**, 3017 (2013).